

# Evolution of Magnetic Field Generated by the Kelvin-Helmholtz Instability

M. Modestov,<sup>1</sup> V. Bychkov,<sup>2</sup> G. Brodin,<sup>2</sup> M. Marklund,<sup>2,3</sup> and A. Brandenburg<sup>1,4</sup>

<sup>1</sup>*Nordita, KTH Royal Institute of Technology and Stockholm University,  
Roslagstullsbacken 23, SE-10691 Stockholm, Sweden*

<sup>2</sup>*Department of Physics, Umeå University, SE-901 87 Umeå, Sweden*

<sup>3</sup>*Department of Applied Physics, Chalmers University of Technology, SE-41296 Gothenburg, Sweden*

<sup>4</sup>*Department of Astronomy, Stockholm University, SE-10691 Stockholm, Sweden*

The Kelvin-Helmholtz instability in an ionized plasma is considered with a focus on the generation of magnetic field via the Biermann battery mechanisms. The problem is studied through direct numerical simulations of two counter-directed flows in 2D geometry. The simulations demonstrate the formation of eddies and their further interaction resulting in a large single vortex. At early stages, the generated magnetic field evolves due to the baroclinic term in the induction equation, revealing significantly different structures from the vorticity field, despite the fact that magnetic field and vorticity obey identical equations. At later times, the magnetic field exhibits complex behavior and continues to grow even after a hydrodynamic vortex has developed.

## INTRODUCTION

The Kelvin-Helmholtz (KH) instability is one of the most important, fundamental and powerful phenomena in fluid mechanics and plasma physics. The instability develops at the interface between two fluids (gases, plasmas), when one component is gliding along the other. The most important outcome of the KH instability in nature is the generation of turbulence via cascades of interacting vortices. Various examples of the KH instability may be encountered in geophysical and astrophysical flows, from ocean surface waves excited by wind, turbulent jets and wakes, up to large-scales instabilities in the interstellar medium, accretion discs and supernova remnants [1–3]. Presently, there is also growing interest in the KH instability in the context of inertial confinement fusion (ICF) [4–8]. Initially, interest in the KH instability has been fueled by research focusing on the Rayleigh-Taylor (RT) instability, which has been one of the most actively explored problems within the ICF applications for decades. At the nonlinear stage of the RT instability, light fluid (pushing or supporting a heavy one) forms bubbles rising “up”, with spikes of heavy matter falling “down” in a real or effective gravitational field [9–12]. The relative motion of light and heavy components results in a secondary KH instability with subsequent generation of turbulence and possible mixing of the two substances. The well-known mushroom structure of the RT bubbles is, in fact, the outcome of a secondary KH instability.

However, lately, a large number of papers have addressed the ICF related KH instability for its own sake without direct relation to the RT instability [4–8, 13]. A good deal of experiments have been designed and performed on the Omega Laser Facility focusing on the KH instability, e.g., at the foam-aluminum interface in a layered target with two different substances set in motion by counter-propagating shock waves [8]. The other option was inducing the KH instability by a shock refracted at

an interface separating two substances of noticeably different density [5–7]. The purpose of these experiments was typically to study generation of vortices and turbulence at the KH unstable interface. There has also been much interest in the RT and KH hydrodynamic instabilities as sources of magnetic field in plasmas. Several mechanisms of magnetic field generation in plasmas have been proposed, including thermo-electric and baroclinic effects, the ponderomotive force from an inhomogeneous laser beam, and some others [14–17].

Under extreme ICF conditions, plasma motion is expected to produce an ultra-high magnetic field, which may alter the plasma flow dynamics as well as influence background magnetic and electric fields. The earliest measurements of magnetic field produced by laser plasma were made already in seventies, detecting kilogauss field strength [14, 18]. Modern powerful laser setups stimulate experimental activity during the last few years in this area. Recent experiments on the RT instability at the OMEGA laser facility demonstrated generation of magnetic field with values up to 1 MGauss [19–21]. In order to obtain thorough knowledge of the KH instability phenomenon, a special setup has been designed and built within the OMEGA facilities [4]. Unfortunately, so far, experiments on the laser-driven KH instability have been performed without direct measurements of the instability-generated magnetic field [4–8, 13].

Much work has also been done on numerical simulations of both the RT and KH instabilities, taking into account the resulting magnetic field generation [22–25]. However, until now, all numerical investigations have been for strongly oversimplified model flows, such as the classical 2D RT instability at an inert interface [22–24], which is far away from realistic ICF conditions. Simulations of the KH instability in laser plasma have also been performed, but they did not take into account the magnetic field generation [7]. Only recently, magnetic field generation by the KH instability has been considered in the astrophysical context [25]. However, those studies

have been performed within the kinetic, not magneto-hydrodynamic (MHD) approach, for the specifically astrophysical cold-fluid KH perturbations and electron-ion shear flows.

The purpose of the present paper is to investigate generation and evolution of the magnetic field arising from the KH instability due to the Biermann battery effect. Analytical treatment of the full set of MHD equations is extremely difficult due to the nonlinear terms, although linear stability analysis may provide necessary estimates for further experiments and computer studies. By contrast, direct numerical simulations are a more powerful tool, which provides a complete picture of the plasma dynamics. For this work we have performed numerical simulations of the magnetic KH instability using the PENCIL CODE [26, 27]. We consider two counter-directed flows of conducting plasma in 2D domain which is a natural setup for the KH studies similar to the Omega Laser facility experiments [4–8]. First of all, we show that the KH instability does generate magnetic field due to a baroclinic term in the induction equation. We observe and discuss the dynamics of the generated magnetic field and the vorticity field in the flow. In contrast to previous studies of the RT instability with magnetic field generation [22–24], we show that the behavior of magnetic field and vorticity in the flow may be qualitatively different. In particular, the magnetic field may yield complex structures influenced by secondary KH instabilities at smaller scales. Our simulations show that the magnetic field continues to grow even after the hydrodynamic vortex has been developed and started decaying due to non-zero plasma viscosity. The results obtained demonstrate that the relation between vorticity and magnetic field in the MHD instabilities is not as straightforward, as it was believed previously, and indicate wide prospects for future research, including both experimental, theoretical and numerical approaches.

## THE BASIC PLASMA MODEL EQUATIONS AND THE NUMERICAL METHOD

In order to study magnetic field generation owing to the KH instability, we solve the compressible MHD equations for a visco-resistive plasma that is fully ionized. The magnetic field is resolved in terms of the magnetic vector potential  $\mathbf{B} = \nabla \times \mathbf{A}$ , thus ensuring zero divergence of  $\mathbf{B}$ . Specific entropy is used instead of temperature. Thus, the governing equations of plasma dynamics are

$$\frac{D \ln \rho}{Dt} = -\nabla \cdot \mathbf{u}, \quad (1)$$

$$\frac{D \mathbf{u}}{Dt} = -\frac{1}{\rho} \nabla p + \frac{1}{\rho} \mathbf{J} \times \mathbf{B} + \frac{1}{\rho} \nabla \cdot 2\nu \rho \mathbf{S}, \quad (2)$$

$$\frac{\partial \mathbf{A}}{\partial t} = \mathbf{u} \times \mathbf{B} - \eta \mu_0 \mathbf{J} + \beta \frac{1}{\rho} \nabla p, \quad (3)$$

$$\frac{Ds}{Dt} = \frac{1}{\rho T} \nabla \cdot (K \nabla T) + \frac{1}{\rho T} \eta \mu_0 \mathbf{J}^2 + \frac{1}{T} 2\nu \mathbf{S}^2, \quad (4)$$

where  $D/Dt = \partial/\partial t + \mathbf{u} \cdot \nabla$  is the advective time derivative,  $\rho$  is the plasma density,  $\mathbf{u}$  is the velocity,  $p$  stands for the pressure,  $\mathbf{J} = \mu_0^{-1} \nabla \times \mathbf{B}$  is the current density,  $\nu$  and  $\eta$  are the kinematic viscosity and magnetic diffusivity, respectively,  $K$  is the thermal conductivity,  $\mathbf{S}$  is the strain tensor,

$$S_{ij} = \frac{1}{2} \left( \frac{\partial u_i}{\partial x_j} + \frac{\partial u_j}{\partial x_i} - \frac{2}{3} \delta_{ij} \nabla \cdot \mathbf{u} \right), \quad (5)$$

$\beta = m_p/e$  is the proton mass to charge ratio,  $T$  is temperature, and  $s$  is the specific entropy. The ideal gas equation complements Eqs. (1)–(4), so that the pressure is given by  $p = \frac{1}{\gamma} \rho c_s^2$ , where  $\gamma = c_P/c_V = 5/3$  is the ratio of specific heats at constant pressure and volume, respectively, the sound speed is a function of density and entropy defined as  $c_s^2 = c_{s0}^2 \exp[\gamma s/c_p + (\gamma - 1) \ln(\rho/\rho_0)]$ , and  $c_{s0}$  and  $\rho_0$  are normalization constants. The last term in the induction equation (3) is identical to the baroclinic term in the vorticity equation; see Eq. (10) below. It represents the Biermann battery mechanism, which acts as a source of magnetic field generation.

The set of equations (1)–(5) has been solved with the help of the PENCIL CODE [26, 27], based on sixth-order finite difference spatial derivative approximations and a third order Runge-Kutta scheme for time stepping. The code is primarily used to solve 3D problems, such as turbulent solar dynamo evolution in Cartesian, spherical or cylindrical coordinates. In addition, for efficient massive calculations the MPI parallelization can be used in all three directions. The upper and lower walls are assumed to be impenetrable stress-free boundaries with a perfect conductor conditions for the magnetic vector potential, i.e.,

$$\begin{aligned} u_y &= 0, & \partial u_x / \partial y &= 0, \\ A_y &= 0, & \partial A_x / \partial y &= 0. \end{aligned} \quad (6)$$

In the other directions we use periodic boundary conditions. In all the simulations presented below we use  $1152^2$  meshpoints.

The KH instability is essentially a 2D phenomenon, so that its main features may well be studied in two dimensions. Taking into account 3D geometry one is faced with turbulent mixing in the transverse direction to the initial flow plane. This may conceal important physical properties of the instability and makes it computationally expensive and harder to investigate. Moreover, considering magnetic fields in 3D, there is inevitably magnetic dynamo action, which affects the evolution of the magnetic field [28]. In a 2D flow, magnetic fields originate from the Biermann battery only, while the MHD dynamo (the

first term of the rhs of Eq. (3)) does not operate in this case. The Ohmic term describes the decay of magnetic field due to magnetic diffusivity.

In our studies we use a single fluid description with two layers of slightly different density. Basically, the KH instability requires an interface with only velocity shear, while density may be either different or the same for both layers. The linear stability analysis for infinitesimal perturbations  $y = y_0 + f(x, t)$  with  $f(x, t) \propto \exp(\sigma t + ikx)$  for the inviscid case predicts the KH instability growth rate as [29]

$$\sigma = \frac{2\sqrt{\Theta}}{1 + \Theta} kU_0 - \frac{\Theta - 1}{\Theta + 1} kU_0 i, \quad (7)$$

where  $\Theta = \rho_{\max}/\rho_{\min} > 1$  is the density ratio of the two layers,  $k$  is the perturbation wavenumber, and the plasma in the two layers moves with velocities  $u_x = \pm U_0$ . The dispersion relation (7) includes both real and imaginary parts, although the former term is much larger than the latter one in our simulations (see below),  $\text{Im}[\sigma]/\text{Re}[\sigma] \approx 0.02$ . As we can see, the largest growth rate corresponds to the case of equal densities of the two layers,  $\Theta = 1$ . The Biermann battery term generates magnetic field when the pressure and density gradients are not collinear. In highly compressible flows, the density gradient may arise through plasma compression. However, within this paper we limit ourselves to an almost incompressible case; compressibility effects will be discussed in further works. For this reason, we use  $\Theta \approx 1.02$ , thus ensuring a powerful KH instability and a finite density gradient at the interface. A higher density ratio leads to larger gradients and a stronger effect of the Biermann battery, even though it does reduce the KH instability strength. In addition, we solve the entropy equation, Eq. (4), which may also be considered as an equation for temperature; it is responsible for the obliqueness between pressure and density gradients. For nearly isobaric flows, pressure variations arise from flow compressibility at small but finite Mach numbers. Hence the initial conditions for the simulations may be summarized as follows

$$u_x/c_{s0} = 0.01 \tanh(y/d) = \ln \rho/\rho_0 = -s/c_P, \quad (8)$$

where  $d$  is the interface thickness, which allows a continuous transition between the two layers. The other component of  $\mathbf{u}$  and all components of  $\mathbf{B}$  are set to zero initially. The initial entropy distribution is computed in a way to have constant pressure in the whole domain, so that the temperature is inversely proportional to the density. In order to trigger the instability we add velocity perturbations to initial distribution. We use two types if initial perturbations as white noise and sinusoidal perturbations for  $y$  component of the velocity field.

## Parameters set

The MHD description of the KH instability involves many parameters that may influence the evolution of the magnetic and velocity fields. The whole parameter set in dimensionless form with the typical values used in our simulations is listed below

$$\begin{aligned} \text{Ma} &= U_0/c_s = 0.01, \\ \text{Re} &= U_0 L/\nu \approx 10^3, \\ \text{Re}_M &= U_0 L/\eta = \text{Re}, \\ \text{Pr} &= \nu/\kappa = 1, \\ \Theta &= 1.02, \end{aligned} \quad (9)$$

which are the Mach, Prandtl, and Reynolds numbers, the density ratio, the magnetic Reynolds number, respectively. Here,  $\kappa = K/\rho c_P$  is the thermal diffusivity. From a hydrodynamic point of view, the main parameters of the KH instability are the Mach and Reynolds numbers. The Mach number quantifies the compressibility effect; it also characterizes the time scale of the process relative to the acoustic time scale. In this paper we use a rather small value of the Mach number, representing an almost incompressible flow. The Reynolds number determines also the smallest length scale accessible and is also a limiting factor from a numerical point of view. At high Reynolds numbers, the flow becomes turbulent. In order to have reliable results for a turbulent flow, one has to resolve the Kolmogorov length scale, which increases dramatically the numerical resources demanded for the study. The Prandtl number characterizes the relative role of viscous and thermal effects of the flow. For the sake of numerical stability the Prandtl number is always set to unity in our simulations. The density ratio of the two layers determines the growth rate of the perturbations in the linear stage. In experiments the actual value of the density ratio may reach several hundreds for ICF conditions, posing an obstacle for numerical simulations. At the same time, the density ratio was quite moderate for the KH experiments at the OMEGA laser facility being comparable to unity [4–8]. In this paper we also use moderate values of this factor slightly above unity so we can use the density for visualizing the process.

In a magnetized plasma, one additional parameter is involved in the simulations, namely the magnetic Reynolds number. It characterizes the decay of magnetic field due to a finite plasma conductivity. For simplicity and the sake of numerical stability we always keep the magnetic Reynolds number equal to the flow Reynolds number. In addition, the hydrodynamic parameters mentioned above may also influence the generation of magnetic field in a critical way. For example, flow compressibility is expected to affect the magnetic field evolution as it provides an additional contribution to the Biermann battery term. Besides, the density gradient plays a governing role for the magnitude of the generated magnetic field, so that the density ratio becomes an important pa-

parameter for proper quantitative estimates.

In this paper we focus on some universal features of magnetic field generation and its further evolution due to the KH instability. For this reason we keep all the parameters fixed for all the simulations, using a moderate value for the Reynolds number,  $Re \approx 10^3$ , to avoid a strongly turbulent flow. However, it is not too low either, so as to avoid fast viscous damping of the KH instability.

## RESULTS

In the simulations we may distinguish several stages in the development of the KH instability. In the linear stage, all perturbed values grow exponentially – in agreement with the dispersion relation Eq. (7). At this stage the interface between the layers acquires a sinusoidal shape of small amplitude, which also grows exponentially in time. During the second stage, the amplitude continues to grow forming a number of smaller vortices, see upper panel of Fig. 1. Later, the vortices interact with each other and merge into a single vortex of the largest possible size allowed by the system geometry, as shown in Fig. 1. In order to observe such interacting vortices, we have performed a simulation with  $Re = 2000$ ; the corresponding sequences of density and vorticity are demonstrated in Fig. 1. After that the large-scale vortex decays due to viscosity if no external forcing is applied to support the vorticity. We can also observe a minor drift of the vortex core due to non-zero  $\text{Im}[\sigma]$  in Eq. (7). In the case of high Reynolds numbers, the third stage may turn into turbulent mixing of the flows leading to isotropic turbulence as the final outcome of the KH instability. In this paper we consider the whole process of the instability development, though paying particular attention to the early stages. In all the simulations presented below we use a smaller Reynolds number ( $Re = 1000$ ), in order to avoid possible turbulent behavior and to ensure proper resolution.

Focusing on the magnetic field generation, we naturally expect the field to have a similar structure as the vorticity of the flow. Analytically the evolution of vorticity and the magnetic field are described by equations of the same mathematic form; by taking curl of Eqs (2) and (3) one ends up with

$$\frac{\partial \mathbf{B}}{\partial t} = \nabla \times (\mathbf{u} \times \mathbf{B}) - \beta \frac{\nabla \rho}{\rho^2} \times \nabla p + \eta \nabla^2 \mathbf{B}, \quad (10)$$

$$\frac{\partial \boldsymbol{\omega}}{\partial t} = \nabla \times (\mathbf{u} \times \boldsymbol{\omega}) + \frac{\nabla \rho}{\rho^2} \times \nabla p + \nu \nabla^2 \boldsymbol{\omega}. \quad (11)$$

Based on this analogy, one might be tempted to deduce that the magnetic field is linearly proportional to the vorticity field. In particular, such a relation between vorticity and the magnetic field has been demonstrated in the simulations of the RT instability in magnetized

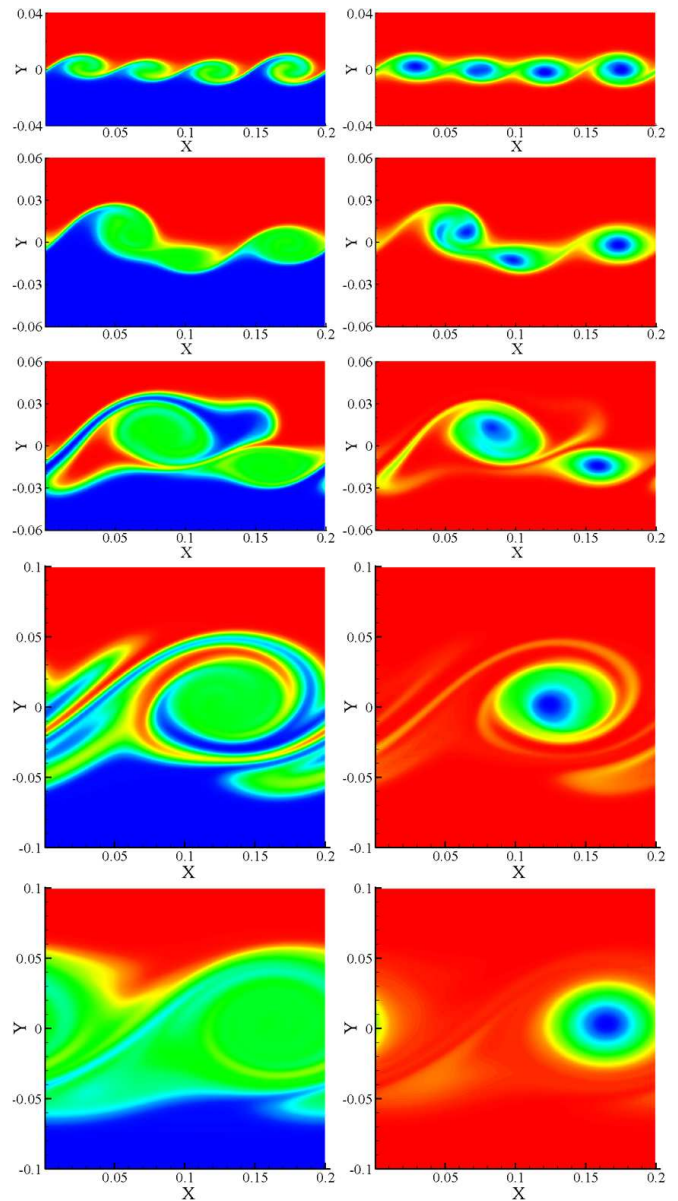


FIG. 1: Density (left panel) and vorticity (right panel) evolutions for the white noise simulation with  $Re = 2000$  for time instants  $t = 2\tau_0; 3\tau_0; 4.5\tau_0; 7.5\tau_0; 12\tau_0$ .

plasma [23, 24]. By contrast, in our simulations the generated magnetic field has significantly different structure as compared to the vorticity, see Figs. 2–9. This difference stems primarily from different initial conditions for these two quantities in our simulations; these different initial conditions are expected to be rather universal for the KH plasma experiments [5–8]. At the initial time instant, we take zero magnetic field everywhere in the domain, while vorticity has inevitably a certain non-zero distribution due to the initial velocity profile forming the two counter-flows; see in Fig. 2. As a result of this difference in the initial conditions, the evolution of the magnetic field is mostly governed by the second term on the

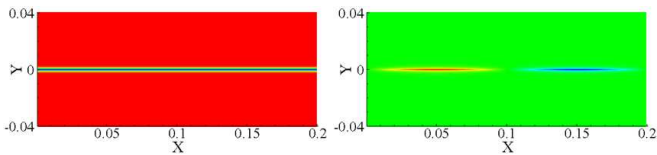


FIG. 2: Initial vorticity field (left) and velocity perturbation of  $u_y$  (right) for a single mode simulation.

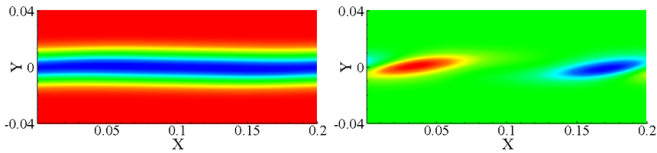


FIG. 3: Distribution of vorticity (left) and magnetic field  $B_z$  (right) at the linear stage,  $t = 3\tau_0$ .

right hand side of Eq. (10), while the first term can be neglected. In the case of the vorticity equation (11), the situation is the opposite with the first term dominating over the baroclinic one.

As mentioned above, we use two types of initial perturbations, a sinusoidal one and white noise. Below, we consider them one by one, starting from a single mode perturbation and finishing by the white noise.

### Single-mode perturbations

A single-mode perturbation as initial condition is simple and allows a more accurate investigation and thorough understanding of the processes during the early stages of the instability evolution. The initial perturbation for the transverse velocity component represents a wave of one period with the amplitude exponentially decaying to the outer walls,

$$u_y = \tilde{u}_y \sin(kx) \exp(-|y|/w),$$

where  $k = k_0 = 2\pi/D$ , is the perturbation wavenumber,  $D$  is the length of the domain and  $w$  is the interface width. During the linear stage the instability evolution can be demonstrated by the generation of the magnetic field, as depicted in Fig. 3. The single mode leads to the slowest growth rate of the instability, so that after three turnover times,  $t = 3\tau_0$  ( $\tau_0 = L_0/U_0$ ), the perturbations are still almost linear. The distribution of vorticity is slightly changed in terms of bending, however it becomes much wider at the flow interface. During the linear stage of the instability, two regions of opposite magnetic field orientation have formed near the humps of the flow interface. From Fig. 3 we clearly see that the generated magnetic field has quite a different structure compared to the vorticity field, which has been discussed above. It should be noted that the color maps for vorticity and magnetic field also differ. Initially, the vorticity is almost

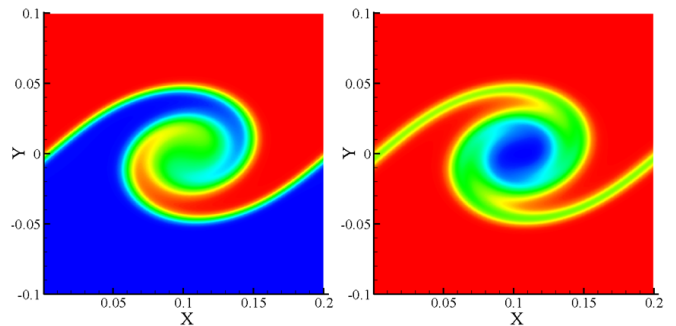


FIG. 4: Density (left) and vorticity (right) for  $t = 6\tau_0$ .

zero in the hole domain (shown as red), while in the middle region it reaches a certain negative value, depicted in dark blue. The  $z$  component of the magnetic field takes negative (blue) and positive (red) values; this coloring is also used for all other figures.

The perturbations grow further, revealing the typical picture of a wave breaking phenomenon and forming a single vortex. In Fig. 4 we present the distribution of density and vorticity at  $t = 6\tau_0$ . As expected, we observe the formation of a large vortex with a characteristic structure. During this stage the magnetic field exhibits more interesting behavior. When the two fluids start mixing, additional regions with large density gradients appear, leading to a spiral structure of the magnetic field. It continues evolving mostly due to the Biermann battery term, although nonlinear effects become more visible at this stage. We demonstrate magnetic field structure together with the baroclinic term in Fig. 5 for several time instants. On the left, visualizations of the magnetic field and the baroclinic term have very similar distributions. For these time instants, the last term of Eq. (10) is dominating over the others and governs the evolution of the magnetic field. After a short time the structure of the baroclinic term exhibits separated islands of different signs, following density evolution. The magnetic field tends to be continuous due to convective term in Eq. (10), which results in a swirling structure of the magnetic field. However the baroclinic term remains dominating in the magnetic field generation. In the last time instant presented in Fig. 5, we see spiral waves in the magnetic field structures. To make sure that the spiral waves do not stem from poor resolution, additional simulations with higher resolution have been performed. These runs suggest that the spiral structures originate from physical effects, e.g. the interference of several magnetic field sources located in different places or a secondary instability leading to spiral patterns as one can find in nonlinear physics [30–32]

Another interesting feature, which is observed in all the simulations and is in stark contrast to the decaying vortex, is that the magnitude of the magnetic field continues to grow during the whole process, as shown

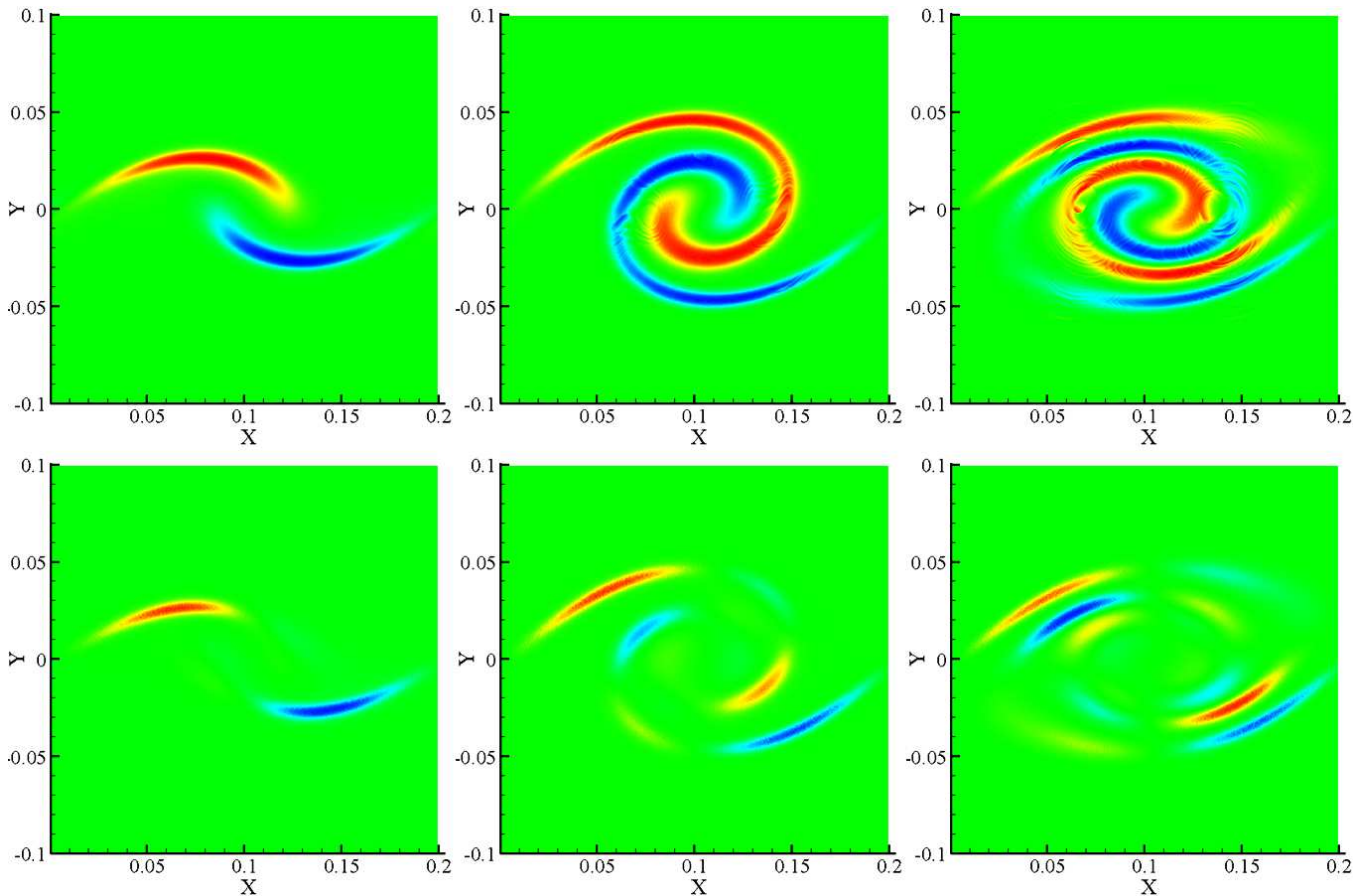


FIG. 5: Magnetic field structure (upper panel) and corresponding baroclinic term (lower panel) at  $t = 5\tau_0$ ;  $6\tau_0$ ;  $7\tau_0$  respectively.

in Fig. 6. Qualitatively it may be understood in the following way. The Biermann term evolves due to non-collinearity of density and pressure gradients. As it is shown in Figs. 7 and 8, at late stages of the process this term acquires a certain structure with small, but finite magnitude, which remains almost constant. Hence, the magnetic field has always a source supporting its continuous growth. In Fig. 6, we also plot the time evolution of the averaged values of the positive constituents of the baroclinic term and velocity  $u_y$ . In order to present all the values in one plot, velocity and baroclinic term have been scaled to their maximal values; the magnetic field is scaled by  $\beta\langle\omega_z\rangle$ , which would be the field strength if both  $B_z$  and  $\omega_z$  were solely caused by the baroclinic term. Here,  $\langle\omega_z\rangle$  is the mean vorticity at the end of the run at  $t = 20\tau_0$ . Thus, if  $\omega_z$  was caused by the baroclinic term,  $\langle B_z\rangle/\beta\langle\omega_z\rangle$  would be unity. Remarkably, even though most of the contribution to  $\omega_z$  comes from the shear flow, this ratio still reaches values of about 0.1. During the first stage, all quantities grow exponentially in a similar way. Initially, a non-zero value of the battery term is due to sharp density gradient coupled with velocity perturbations. As the instability develops, the velocity reaches its maximal value at  $t \approx 6\tau_0$  and starts decaying. The

baroclinic term shows similar behavior, but it decays to some small but finite level. This value is a few orders of magnitude smaller than the initial vorticity, so that it cannot produce additional vorticity to sustain the vortex. It is, however, enough to sustain the growth of magnetic field, as shown in Figs. 6 and 7. At a much later stage,

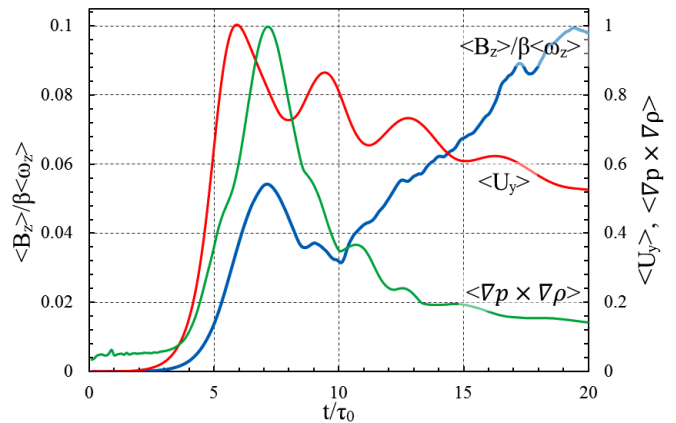


FIG. 6: Time evolution of the scaled averaged quantities representing magnetic field, baroclinic term and velocity  $u_y$ .

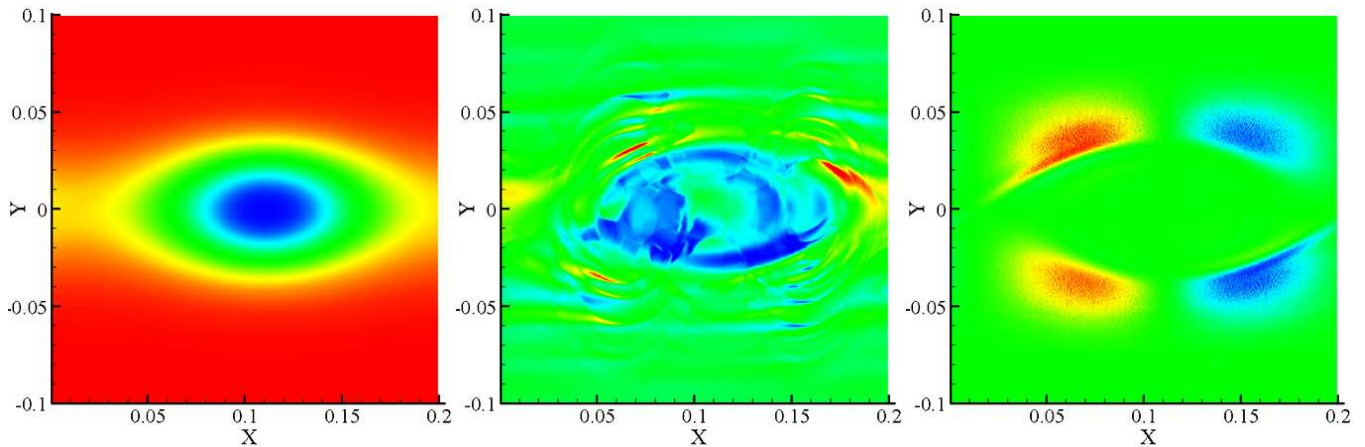


FIG. 7: Distribution of vorticity (left), magnetic field (middle) and baroclinic term (right) in the very later stage of the KH instability,  $t = 20\tau_0$ .

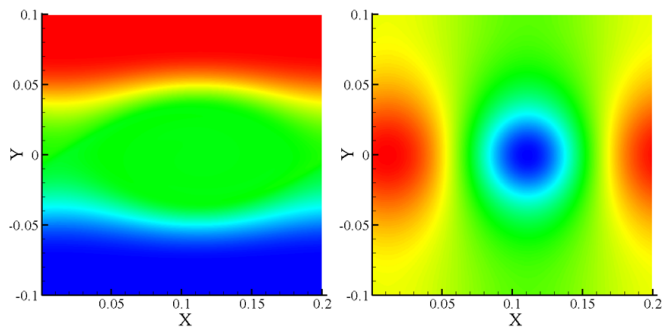


FIG. 8: Distributions of density (left) and pressure (right) corresponding to the previous picture.

the instability demonstrates a well-developed single vortex, which decays slowly due to viscosity; see Figs. 7 and 8. Basically a single vortex corresponds to a circular distribution of the flow vorticity. The elongated shape in Fig. 7 is a result of the initial flow influence, which stretches the vortex in line with the flow. The magnetic field structure is very different from that of both vorticity and the baroclinic term; it is an outcome of the continuous generation due to the Biermann battery, its probable interference and convective transfer by the flow. This phenomenon is not properly understood yet and demands further investigation well beyond the scope of the present paper. Still we may admit that inside the vortex there is a region of negative magnetic field concentration, which resembles the vorticity field. The baroclinic term is a consequence of the spatial properties of flow density and pressure. For a better understanding of its structure they are presented in Fig. 8, which demonstrates a mixing layer with an almost homogeneous density distribution inside the vortex. However the upper and lower parts of the domain are still filled with unmixed components, so that there are two regions with noticeable density gradient. The pressure picture of the vortex is governed

by the hydrodynamical contribution, as the flow remains isobaric in total. There is a certain pressure minimum in the vortex core, due to flow compressibility; the pressure variations do not exceed the  $\text{Ma}^2$  estimate.

### Several-modes perturbations

The single-mode simulations demonstrate basic features of the KH instability together with the magnetic field generated by the plasma motion. According to the dispersion relation (7), smaller vortices with larger wavenumbers grow faster than a single vortex of the largest possible size. In order to study the evolution of multiple vortices in the KH instability, we have performed several simulation runs with larger wavenumbers of initial perturbations. In particular, we have used  $k/k_0 = 2, 3,$  and  $4$  in order to see the development of

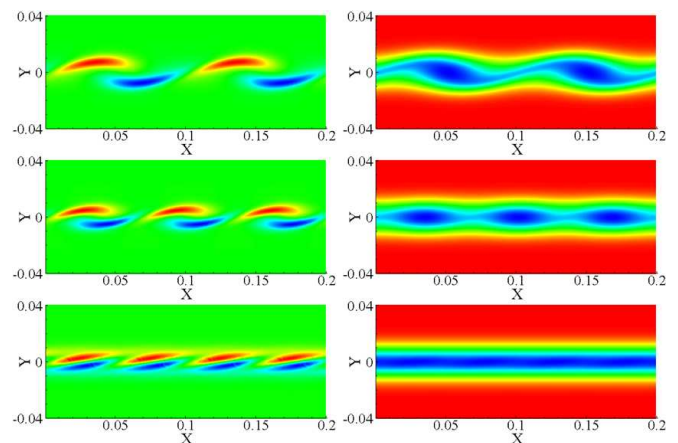


FIG. 9: Magnetic field (left panel) and vorticity (right panel) at time instant  $t = 3\tau_0$  for initial perturbation of  $k = 2k_0; 3k_0; 4k_0$ .

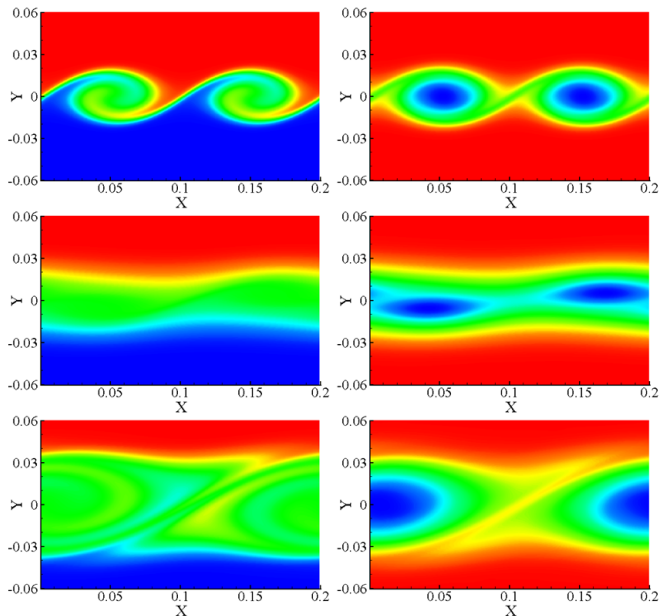


FIG. 10: Density (left panel) and vorticity (right panel) evolutions during merging of two eddies for  $k = 2k_0$ , time moments correspond to  $t/\tau_0 = 4, 10$ , and  $15$ .

several vortices. In these simulations the growth of individual vortices resembles the evolution of a single vortex described in the previous section. As expected, the magnetic field generation occurs faster, which is due to the larger growth rate indicated by the dispersion relation. The early stages of vortex formation are depicted in Fig. 9 by means of magnetic field and vorticity distributions. The vortices can be seen both in magnetic field and vorticity, although the magnetic field represents the vortex location more clearly, while vorticity has a very smooth profile.

After that we observe the interaction of vortices, which may be regarded as a transient in the evolution from multiple small-scale vortices to a single large vortex of maximal possible size. These smaller vortices at the KH-unstable interface represent a mixing layer rather than separately spinning eddies; this effect becomes obvious for perturbations of high wavenumbers. Merging of vortices takes place in a mixing layer in a smooth manner; we demonstrate it by showing the vorticity for case  $k = 2k_0$  in Fig. 10. At the final stage of a single vortex all the quantities have similar structures to those depicted in Figs. 7 and 8.

#### White noise perturbation

Finally, we consider the evolution of the magnetic KH instability with white noise initial perturbations in velocity. Such conditions allow the system to choose its own characteristic wavenumber. Actually, the KH instability

develops from the smallest vortices, which can be resolved by the simulation, as its dispersion relation Eq. (7) does not imply any suppression in the high wavenumber range [29]. We study the evolution of the instability by monitoring the magnetic field at three times,  $t/\tau_0 = 1, 2$ , and  $4$ ; see Fig. 11. At the early stage, regions of different sign of the magnetic field indicate the location and number of vortices. We see that small vortices grow and interact with each other simultaneously until two eddies are formed. Starting from this point, the instability evolution resembles the case with  $k = 2k_0$ , described in the previous section, although it grows faster. In the double mode simulation, two eddies merge into a single vortex for about ten turnover times, while in the white noise run the two eddies merge into a single one after about five turnover times.

The time evolution of the magnetic field is summarized in Fig. 12. It shows the scaled average magnetic field versus time for several types of initial perturbations. Roughly speaking, the magnetic field evolution may be divided into two parts, where the first one corresponds to the exponential growth during the earlier stages of the instability, and the second part represents an almost linear

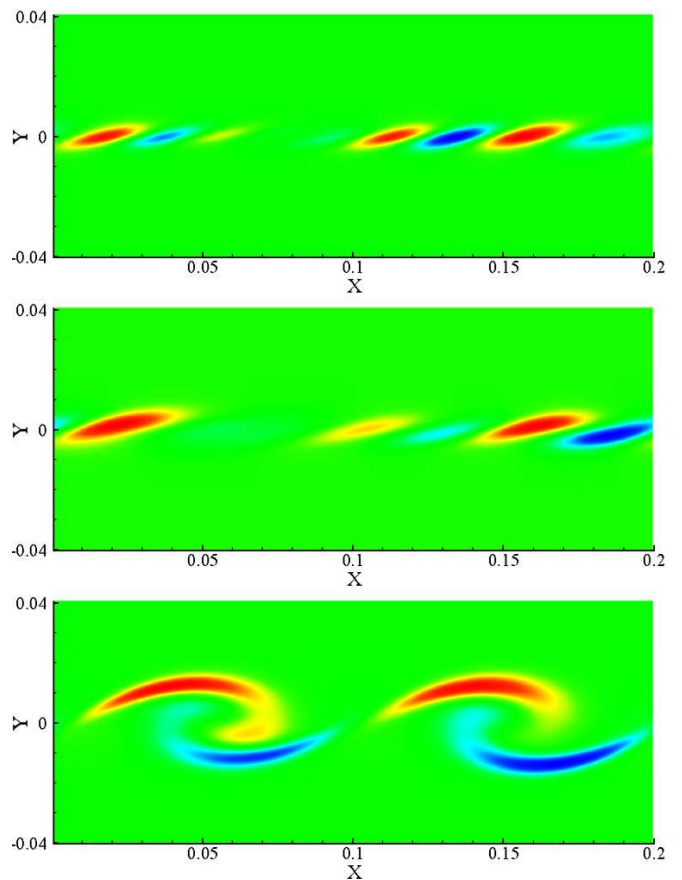


FIG. 11: Magnetic field evolution in the simulation with the white noise initial perturbation at time instants  $t = \tau_0$  (top),  $t = 2\tau_0$  (middle) and  $t = 4\tau_0$  (bottom).

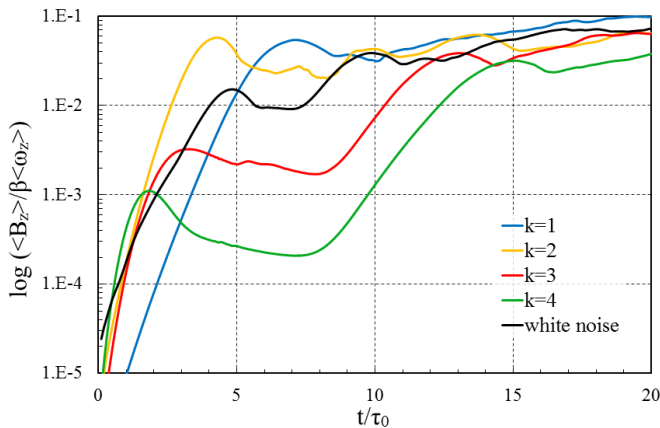


FIG. 12: Magnetic field evolution versus time for different initial perturbations in logarithmic scale.

growth at the later stages of the process. In this figure with the logarithmic scale we see that the magnetic field grows faster for larger wavenumbers of the initial perturbations according to the linear dispersion relation (7). The white noise perturbation produces weaker growth, which can be explained in the following way. As we have seen in Fig. 11, already at  $t = \tau_0$  there are several small eddies, but an eddy is a nonlinear phenomenon. So we may conclude that the pure linear stage of the KH instability in case of white noise perturbation is extremely short. However, the interaction of small vortices also gives rise to exponential growth of the generated magnetic field.

The magnetic field evolution depicted in Fig. 12 has several interesting features. For all cases, except  $k = k_0$ , there is a certain plateau in the growth of the magnetic field, especially for the cases with  $k \geq 2k_0$ . The plateau corresponds to the period when the mixing layer is formed and, hence, the evolution of the instability slows down and the baroclinic term decreases. In addition, each curve has one or even several pronounced peaks, e.g. at  $t = 5\tau_0$  and  $10\tau_0$  for the white noise case. These peaks correspond to the smaller vortices merging into bigger ones. Qualitatively it may be understood as an increase of the mixing of the two fluids, giving birth to additional slices of different densities. This process leads to the origin of additional areas with non-zero baroclinic term, which resulted in additional generation of the magnetic field.

## CONCLUSIONS

In this paper we have investigated the KH instability in fully ionized plasmas focusing on the generation of magnetic field through the Biermann battery. The instability leads to growth of magnetic field from zero, with no initial seeding. In contrast to the related works on the RT insta-

bility with battery term [23, 24], we have demonstrated that magnetic field and vorticity structures generated by the instability may be quite different, even though they obey similar equations, Eqs. (10), (11). The important difference between magnetic field and vorticity structures originates from intrinsically different initial conditions for these two values, which are supposed to be the common case for the KH plasma experiments [4–8]. Another important finding of the present work is that the magnetic field continues to grow even after the largest vortex has been formed and started decaying. It should be also mentioned that in the present simulations, we take the flow parameters resulting in a relatively weak generated magnetic field, so that it does not affect the hydrodynamic flow. Our results demonstrate that the relation between vorticity and the magnetic field in the MHD instabilities is not as straightforward, as it was believed previously, and indicate wide prospects for future research.

We thank Dhruvadya Mitra and Matthias Rheinhardt for help and useful comments. Financial support from the European Research Council under the AstroDyn Research Project 227952, the Swedish Research Council under the grants 621-2011-5076 and 2012-5797, as well as the Research Council of Norway under the FRINATEK grant 231444 are gratefully acknowledged. We acknowledge the allocation of computing resources provided by the Swedish National Allocations Committee at the Center for Parallel Computers at the Royal Institute of Technology in Stockholm and the National Supercomputer Centers in Linköping, the High Performance Computing Center North in Umeå, and the Nordic High Performance Computing Center in Reykjavik.

- 
- [1] Y. Shen, J. M. Stone, T. A. Gardiner, *ApJ*, **653**, 513 (2006).
  - [2] J. A. Barranco, *ApJ*, **691**, 907 (2009).
  - [3] C.-Y. Wang, R. A. Chevalier, *ApJ*, **549**, 1119 (2001).
  - [4] O. A. Hurricane, *High Energy Density Phys.* **4**, 97 (2008).
  - [5] O. A. Hurricane, J. F. Hansen, H. F. Robey, B. A. Remington, M. J. Bono, E. C. Harding, R. P. Drake, and C. C. Kuranz, *Phys. Plasmas* **16**, 056305 (2009).
  - [6] E. C. Harding et al., *Phys. Rev. Lett.* **103**, 045005 (2009).
  - [7] K. S. Raman, O. A. Hurricane, H.-S. Park, B. A. Remington, H. Robey, V. A. Smalyuk, R. P. Drake, C. M. Krauland, C. C. Kuranz, J. F. Hansen, and E. C. Harding, *Phys. Plasmas* **19**, 092112 (2012).
  - [8] F. W. Doss *et al.*, *Phys. Plasmas* **20**, 012707 (2013).
  - [9] D. Layzer, *Astrophys J.* **122**, 1 (1955).
  - [10] R. Betti and J. Sanz, *Phys. Rev. Lett.* **97**, 205002 (2006).
  - [11] M. Modestov, V. Bychkov, R. Betti, and L.-E. Eriksson, *Phys. Plasmas* **15**, 042703 (2008).
  - [12] V. Bychkov, M. Modestov, V. Akkerman, and L.-E. Eriksson, *Plasma Phys. Contr. Fusion* **49**, B513 (2007).
  - [13] Y. Kuramitsu, Y. Sakawa, S. Dono, C. D. Gregory, S. A. Pikuz, B. Loupias, M. Koenig, J. N. Waugh, N. Woolsey, T. Morita, T. Moritaka, T. Sano, Y. Matsumoto, A.

- Mizuta, N. Ohnishi, and H. Takabe, *Phys. Rev. Lett.*, **108**, 195004 (2012)
- [14] J. A. Stamper, K. Papadopoulos, R. N. Sudan, S. O. Dean, E. A. McLean, and J. M. Dawson, *Phys. Rev. Lett.* **26**, 1012 (1971).
- [15] K. Mima, T. Tajima, and J. N. Leboeuf, *Phys. Rev. Lett.* **41**, 1715 (1978).
- [16] M. G. Haines, *Can. J. Phys.* **64**, 912 (1986).
- [17] J. A. Stamper, *Laser and Particle Beams*, **9**, 841 (1991).
- [18] G. A. Askat'yan, *JETF Lett.* **5**, 93, (1967).
- [19] J. R. Rygg et al, *Science* **319**, 1223 (2008).
- [20] L. Gao, P. M. Nilson, I. V. Igumenshev, S. X. Hu, J. R. Davies, C. Stoeckl, M. G. Haines, D. H. Froula, R. Betti, and D. D. Meyerhofer, *Phys. Rev. Lett.* **109**, 115001 (2012).
- [21] M. J.-E. Manuel, C. K. Li, F. H. Seguin, J. A. Frenje, D. T. Casey, R. D. Petrasso, S. X. Hu, R. Betti, J. Hager, D. D. Meyerhofer, and V. Smalyuk, *Phys. Plasmas* **19**, 082710 (2012).
- [22] B. Srinivasan, G. Dimonte, and X.-Z. Tang, *Phys. Rev. Lett.* **108**, 165002 (2012).
- [23] B. Srinivasan and X.-Z. Tang, *Phys. Plasmas* **19**, 082703 (2012).
- [24] F. Modica, T. Plewa, and A. Zhiglo, *High Energy Density Phys.* **9**, 767 (2013).
- [25] E. P. Alves, T. Grismayer, S. F. Martins, F. Fiza, R. A. Fonseca, and L. O. Silva, *Astrophys. J. Lett.* **746**, L14 (2012).
- [26] <http://pencil-code.googlecode.com>.
- [27] A. Brandenburg and W. Dobler, *Comput. Phys. Commun.* **147**, 471 (2002).
- [28] W. Zhang, A. MacFadyen, and P. Wang, *Astrophys. J.*, **692**, L40 (2009)
- [29] T. Funada and D. D. Joseph, *J. Fluid Mech* **445**, 263 (2001).
- [30] G. Jomaas and C. K. Law, *Phys. Fluids* **22**, 124102 (2010).
- [31] M. Cross, P. Hohenberg, *Rev. Mod. Phys.* **65**, 851 (1993).
- [32] V. Zykov, E. Bodenschatz, *Phys. Rev. Lett.* **112**, 054101 (2014).